MATERIALS SCIENCE

Overcoming immiscibility toward bimetallic catalyst library

Chunpeng Yang[1]*, Byung Hee Ko[2]*, Sooyeon Hwang[3], Zhenyu Liu[4], Yonggang Yao[1], Wesley Luc[2], Mingjin Cui[1], Arnav S. Malkani[2], Tangyuan Li[1], Xizheng Wang[1], Jiaqi Dai[1], Bingjun Xu[2], Guofeng Wang[4], Dong Su[3], Feng Jiao[2†], Liangbing Hu[1†]

Bimetallics are emerging as important materials that often exhibit distinct chemical properties from monometallics. However, there is limited access to homogeneously alloyed bimetallics because of the thermodynamic immiscibility of the constituent elements. Overcoming the inherent immiscibility in bimetallic systems would create a bimetallic library with unique properties. Here, we present a nonequilibrium synthesis strategy to address the immiscibility challenge in bimetallics. As a proof of concept, we synthesize a broad range of homogeneously alloyed Cu-based bimetallic nanoparticles regardless of the thermodynamic immiscibility. The nonequilibrated bimetallic nanoparticles are further investigated as electrocatalysts for carbon monoxide reduction at commercially relevant current densities (>100 mA cm^{-2}), in which $Cu_{0.9}Ni_{0.1}$ shows the highest multicarbon product Faradaic efficiency of ~76% with a current density of ~93 mA cm^{-2}. The ability to overcome thermodynamic immiscibility in multimetallic synthesis offers freedom to design and synthesize new functional nanomaterials with desired chemical compositions and catalytic properties.

INTRODUCTION

Bimetallic nanoparticles have gained broad interest in various fields (*1*, *2*), particularly heterogeneous catalytic reactions such as CO oxidation (*3*), reforming of hydrocarbons (*4*), and transformation of CO_2 to fuel and chemicals (*5*). Distinct from monometallic materials, bimetallic nanoparticles often exhibit unique catalytic properties that cannot be accessed in their constituent metals alone (*6*). For instance, numerous Ni-based bimetallic catalysts modified with metals such as Au and Pt have demonstrated greater resistance against carbon deposition compared with pure Ni in dry reforming of methane (*4*, *7*). However, identifying the origin of the performance enhancement in bimetallic systems remains a fundamental challenge in catalysis, mainly due to the complex nature of the nanostructured bimetallic particles. Many factors, such as the chemical nature of the constituent metals, the size of the particles, and the nanoscale arrangement of the two constituent metals, could play important roles in determining the physicochemical properties (*2*), making it inherently difficult to correlate structures and catalytic behavior (*8*, *9*). Therefore, a general synthetic method that can prepare a broad collection of homogeneously alloyed bimetallic nanoparticles with identical structure is needed to minimize the heterogeneity in bimetallic catalysts.

However, many bimetallic systems do not exist as homogeneous alloys, exhibiting wide miscibility gaps in the phase diagrams due to their positive heat of mixing. For instance, via conventional methods, such as coreduction, concurrent thermal decomposition, seed-mediated growth, and galvanic replacement, bimetallic structures are generally limited to their thermodynamically favorable structures, and syntheses tend to yield core-shell or other heterostructures (*1*, *2*, *10*). While some unconventional methods, such as γ-irradiation (*11*), spark discharge (*12*), pulsed laser ablation (*13*), and surface plasmon resonance (*14*), have been explored to mix immiscible elements, these techniques are dependent on extreme conditions and complex processes or only applicable to specific bimetallic systems.

Here, we report a nonequilibrium synthetic strategy to overcome the immiscibility of bimetallic materials and use Cu-based (Cu-X) bimetallics as a proof of concept to show the successful mixing of bimetallics toward a library of homogeneously alloyed bimetallic nanoparticles. According to binary phase diagrams (*15*), Cu is thermodynamically miscible with metals such as Pd, Zn, etc., but immiscible with other metals such as Ag, Ni, Sn, In, etc., in the composition of $Cu_{0.9}X_{0.1}$ at room temperature (indicated in Fig. 1). Except for those readily miscible systems, Cu does not alloy with most metals via conventional bimetallic synthesis methods but forms various phase-segregated structures, as shown in Fig. 1 (*16*). For example, as Cu and Ag are immiscible at almost all ratios at room temperature, except for a few partially alloyed Cu-Ag bimetallics reported (*5*, *17*, *18*), Cu-Ag bimetallics are generally phase segregated as core-shell, crescent, or other heterostructures, rather than being homogeneously mixed (*19*–*21*).

Nonetheless, nonequilibrium synthesis allows us to freely mix Cu with almost all common metals into homogenous bimetallic nanoparticles without limitation. We then use a collection of Cu-X bimetallic nanoparticles to screen novel catalysts in the electrochemical reduction of carbon monoxide (COR) and study the role of the secondary metals. Among various Cu-X bimetallics, Cu-Ag and Cu-Ni, which have miscibility gaps in their bulk phase diagrams but are homogenously mixed by this nonequilibrium synthesis, show exceptionally high Faradaic efficiencies (FE) of multicarbon (C_{2+}) products at high current densities compared with pure Cu. This nonequilibrium synthesis allows us to generate a library of alloyed bimetallic particles that not only provides an ideal platform for studying the role of secondary metals in reactions of interest but also gives access to a range of novel bimetallic materials that cannot be synthesized through conventional methods.

[1]Department of Materials Science and Engineering, University of Maryland, College Park, MD 20742, USA. [2]Center for Catalytic Science and Technology, Department of Chemical and Biomolecular Engineering, University of Delaware, Newark, DE 19716, USA. [3]Center for Functional Nanomaterials, Brookhaven National Laboratory, Upton, NY 11973, USA. [4]Department of Mechanical Engineering and Materials Science, University of Pittsburgh, Pittsburgh, PA 15261, USA.
*These authors contributed equally to this work.
†Corresponding author. Email: binghu@umd.edu (L.H.); jiao@udel.edu (F.J.)

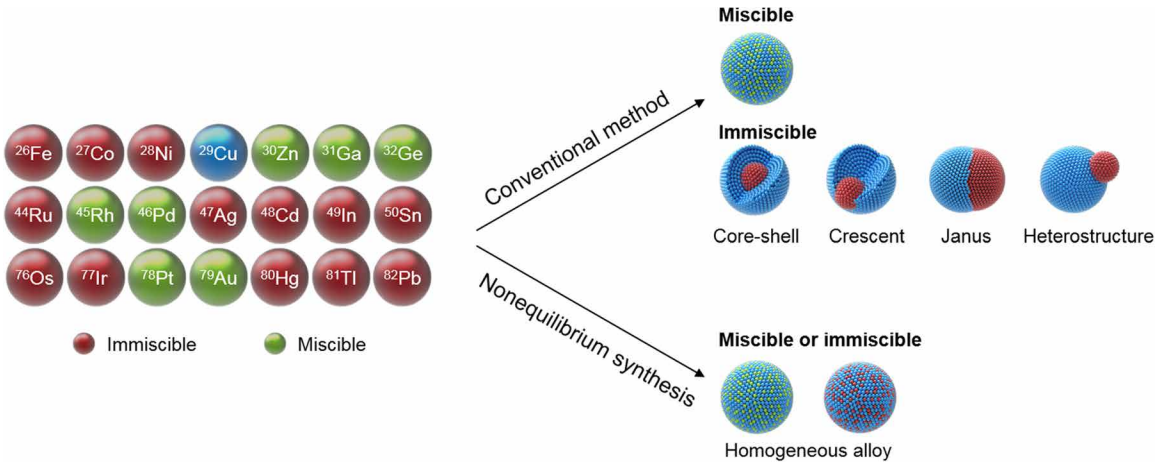

Fig. 1. Synthesis of bimetallic nanoparticles via conventional and nonequilibrium methods. Via conventional bimetallic synthesis methods, only readily miscible metals (shown in green) can mix with Cu, while others (shown in red) form phase-segregated structures (such as core-shell). In contrast, via the nonequilibrium synthesis, Cu and other metals (X) can be kinetically trapped in homogeneously mixed nanoparticles, regardless of their thermodynamic miscibility. The miscibility of Cu and X indicated in the left panel is drawn according to the binary phase diagrams with the composition of $Cu_{0.9}X_{0.1}$ (*15*).

RESULTS

In a typical nonequilibrium synthesis of Cu-Ag bimetallic nanoparticles, we dispersed precursors of two metals [$Cu(NO_3)_2$ and $AgNO_3$] on a carbon substrate [e.g., carbon nanofibers (CNFs) that featured a substantial number of surface defects and functional groups] and treated the material with an ultrashort current pulse (see Materials and Methods for more details) (fig. S1). The heating of the carbon substrate created by the current pulse causes a rapid thermal shock of >1300°C that lasts for only 0.2 s, quickly quenching to room temperature after ceasing the current (Fig. 2A). The metal precursors rapidly decompose during the high-temperature shock and form Cu and Ag atoms mixed together, driven by their mixing entropy at the high temperature. Because of the short duration of thermal shock (~0.2 s), Cu and Ag atoms cannot diffuse across a great distance to form a fully thermodynamically equilibrated phase but instead are kinetically trapped by the surface defects and functional groups of the carbon substrate, forming uniform bimetallic nanoparticles. We observed the uniformity of the morphology and size of the resulting Cu-Ag bimetallic ($Cu_{0.9}Ag_{0.1}$) nanoparticles through scanning electron microscopy (SEM) and transmission electron microscopy (TEM) analysis (Fig. 2, B to D). Energy-dispersive x-ray spectroscopy (EDS) coupled with SEM (fig. S1) confirms the Cu and Ag in the nanoparticles, showing a consistent composition as designed. The metal content of the Cu-Ag bimetallic on the substrate is 17 weight % (wt %) based on a thermogravimetric analysis (fig. S2). The TEM measurement shows that the $Cu_{0.9}Ag_{0.1}$ nanoparticles have an average diameter of 16.7 nm with a very narrow size distribution (Fig. 2E). In contrast, the $Cu_{0.9}Ag_{0.1}$ nanoparticles prepared with the same precursors but via the conventional thermal annealing in a furnace (1000°C in argon flow for 1 hour) show much larger particle size (fig. S3). Another unique feature of the high-temperature shock synthesis is that the resulting nanoparticles are free of surfactants or other residues on surface, which is critical for fundamental heterogeneous catalysis studies.

We further examined the crystalline structure of the $Cu_{0.9}Ag_{0.1}$ nanoparticles synthesized by the nonequilibrium method. The high-resolution scanning transmission electron microscopy (STEM; Fig. 2F) shows that the nonequilibrated $Cu_{0.9}Ag_{0.1}$ bimetallic alloy features a face-centered cubic (fcc) crystalline structure, which is the same as the monometallic Cu and Ag, with $d_{(111)}$ spacing of 2.20 Å. The even Z-contrast in the STEM image (Fig. 2F) indicates a homogeneous, random mixing of Cu and Ag atoms, without phase segregation into a core-shell or other heterostructures. The nonequilibrium synthesized $Cu_{0.9}Ag_{0.1}$ (by thermal shock) showed no segregated phases in the powder x-ray diffraction (XRD) profile (fig. S4), whereas the equilibrium structure of $Cu_{0.9}Ag_{0.1}$ (by conventional thermal annealing) showed notable phase segregation of Cu and Ag. The phase segregation of the equilibrated $Cu_{0.9}Ag_{0.1}$ is clearly observed in the EDS elemental mapping (fig. S5), where Ag is segregated to the surface. By the nonequilibrium synthesis, however, the Cu and Ag atoms in the $Cu_{0.9}Ag_{0.1}$ nanoparticles distribute homogeneously throughout the nanoparticle, as evidenced by EDS elemental mapping (Fig. 2G and additional nanoparticle EDS mappings in fig. S6). EDS line scan across different $Cu_{0.9}Ag_{0.1}$ nanoparticles (fig. S7) further confirms the uniform distribution of Cu and Ag in the nanoparticles obtained by the nonequilibrium method. To investigate the thermal stability of the $Cu_{0.9}Ag_{0.1}$ bimetallic nanoparticles, we performed in situ TEM and EDS line scan using an in situ heating apparatus. As shown in fig. S8, Cu and Ag remained a homogeneous distribution at room temperature, 250°C, and 500°C. When the particle was heated above 750°C, the Ag atoms diffused to the surface. Therefore, the homogeneous mixing of the bimetallic nanoparticles by kinetic trapping is thermally stable up to ~500°C.

In addition to $Cu_{0.9}Ag_{0.1}$ nanoparticles, other $Cu_{0.9}X_{0.1}$ bimetallics, such as $Cu_{0.9}Ni_{0.1}$, $Cu_{0.9}Sn_{0.1}$, $Cu_{0.9}In_{0.1}$, $Cu_{0.9}Pd_{0.1}$, and $Cu_{0.9}Zn_{0.1}$, are also studied. While Ni, Sn, and In are immiscible with Cu at the explored composition ($Cu_{0.9}X_{0.1}$), according to their binary phase diagrams (*15*), we successfully obtained uniform $Cu_{0.9}X_{0.1}$ bimetallic nanoparticles using the nonequilibrium synthetic approach (see SEM and TEM images in figs. S9 to S13). The homogeneity of the resulting $Cu_{0.9}X_{0.1}$ nanoparticles is confirmed by high-angle annular dark-field (HAADF) STEM analysis and the corresponding elemental distribution of Ni, Sn, In, and Pd using EDS (Fig. 2, H to K). The alloyed structures of the $Cu_{0.9}X_{0.1}$ bimetallics are further evidenced by XRD (fig. S14). The $Cu_{0.9}X_{0.1}$ nanoparticles showed similar diffraction patterns with standard Cu, with peak shifts compared with

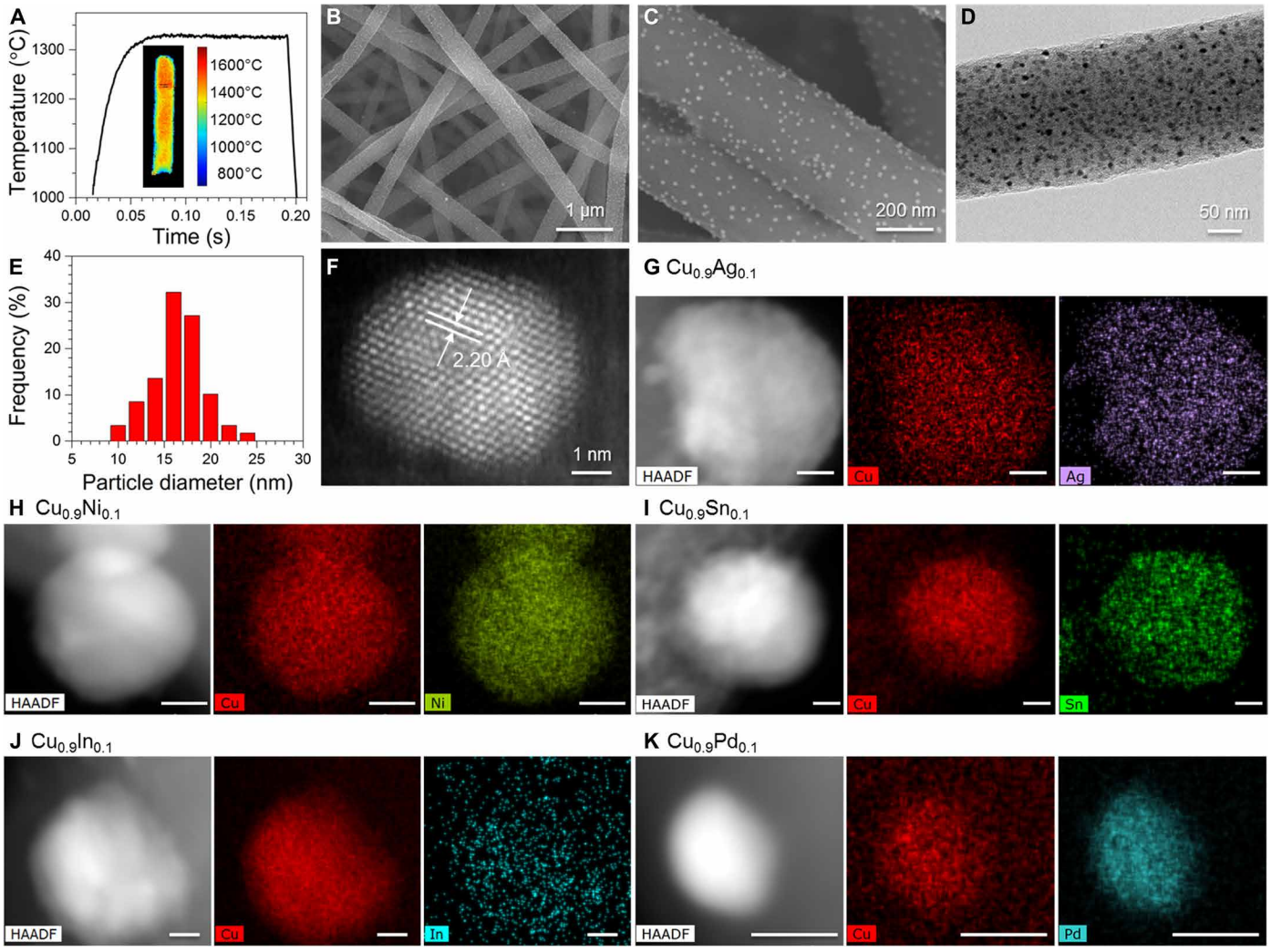

Fig. 2. Nonequilibrium synthesis of Cu-based bimetallic nanoparticles. (**A**) Temperature evolution during the rapid thermal shock process. Inset: Thermal imaging of the substrate at 0.1 s during the high-temperature shock. (**B** and **C**) SEM and (**D**) TEM images of $Cu_{0.9}Ag_{0.1}$ nanoparticles on CNFs. (**E**) Particle diameter distribution of the $Cu_{0.9}Ag_{0.1}$ nanoparticles from the TEM image. (**F**) High-resolution STEM image of the $Cu_{0.9}Ag_{0.1}$ nanoparticles dispersed on the CNFs. HAADF-STEM image and corresponding EDS elemental mapping of (**G**) $Cu_{0.9}Ag_{0.1}$, (**H**) $Cu_{0.9}Ni_{0.1}$, (**I**) $Cu_{0.9}Sn_{0.1}$, (**J**) $Cu_{0.9}In_{0.1}$, and (**K**) $Cu_{0.9}Pd_{0.1}$. Scale bars, 5 nm (G to K).

pure Cu, due to the alloying of Cu and X and changing of lattice parameters. No segregated phase of the secondary metal was observed in the XRD profiles of $Cu_{0.9}X_{0.1}$, demonstrating that the high-temperature shock synthetic approach is a powerful method to overcome the miscibility limitation in bimetallic materials.

We also investigated whether the ratio between two constitute elements can be tuned in the high-temperature shock synthesis. Cu-Ag was chosen as a model system (because of its wide immiscibility gap), and three different compositions of Cu-Ag bimetallic samples (i.e., $Cu_{0.9}Ag_{0.1}$, $Cu_{0.8}Ag_{0.2}$, and $Cu_{0.5}Ag_{0.5}$) were synthesized. The SEM and TEM images of $Cu_{0.9}Ag_{0.1}$, $Cu_{0.8}Ag_{0.2}$, and $Cu_{0.5}Ag_{0.5}$ (Fig. 2, B to D, and figs. S15 and S16) show similar particle size and morphology in all three Cu-Ag bimetallics. The high-resolution STEM images (Fig. 3, A and B) confirm that all three Cu-Ag materials share a similar fcc crystalline structure. The $d_{(111)}$ spacings of the $Cu_{1-x}Ag_x$ (x = 0.1, 0.2, and 0.5) alloys are 2.20, 2.25, and 2.29 Å, respectively, between the $d_{(111)}$ spacings of Cu and Ag metals. The spacing values are higher than those predicted from Vegard's law but show increasing trend with increased Ag content in the $Cu_{1-x}Ag_x$ alloy nanoparticles. Although all three Cu-Ag bimetallics are thermodynamically immiscible (Fig. 3C), homogeneously alloyed Cu-Ag bimetallic nanoparticles are obtained (Figs. 2G and 3, D and E), suggesting that the atomic ratio in bimetallic can be readily tuned in the nonequilibrium synthesis.

To understand the formation of the homogeneously mixed Cu-Ag bimetallic nanoparticles, we conducted atomistic simulations using $Cu_{0.5}Ag_{0.5}$ as a typical immiscible system. We modeled the $Cu_{0.5}Ag_{0.5}$ bimetallic system with a 5-nm-sized cuboctahedral nanoparticle containing 4033 atoms $Cu_{2017}Ag_{2016}$ in an fcc lattice. A Monte Carlo (MC) sampling at high temperature (1000°C) was performed to find a low-energy state. Starting from an atomically dispersed species decomposed from the homogeneously mixed metal nitrate precursors, the atomic configuration of the nanoparticle after MC simulation was quenched to room temperature (fig. S17), without long-range chemical ordering such as phase segregation. To evaluate the stability of the nanoparticle at room temperature, we further performed

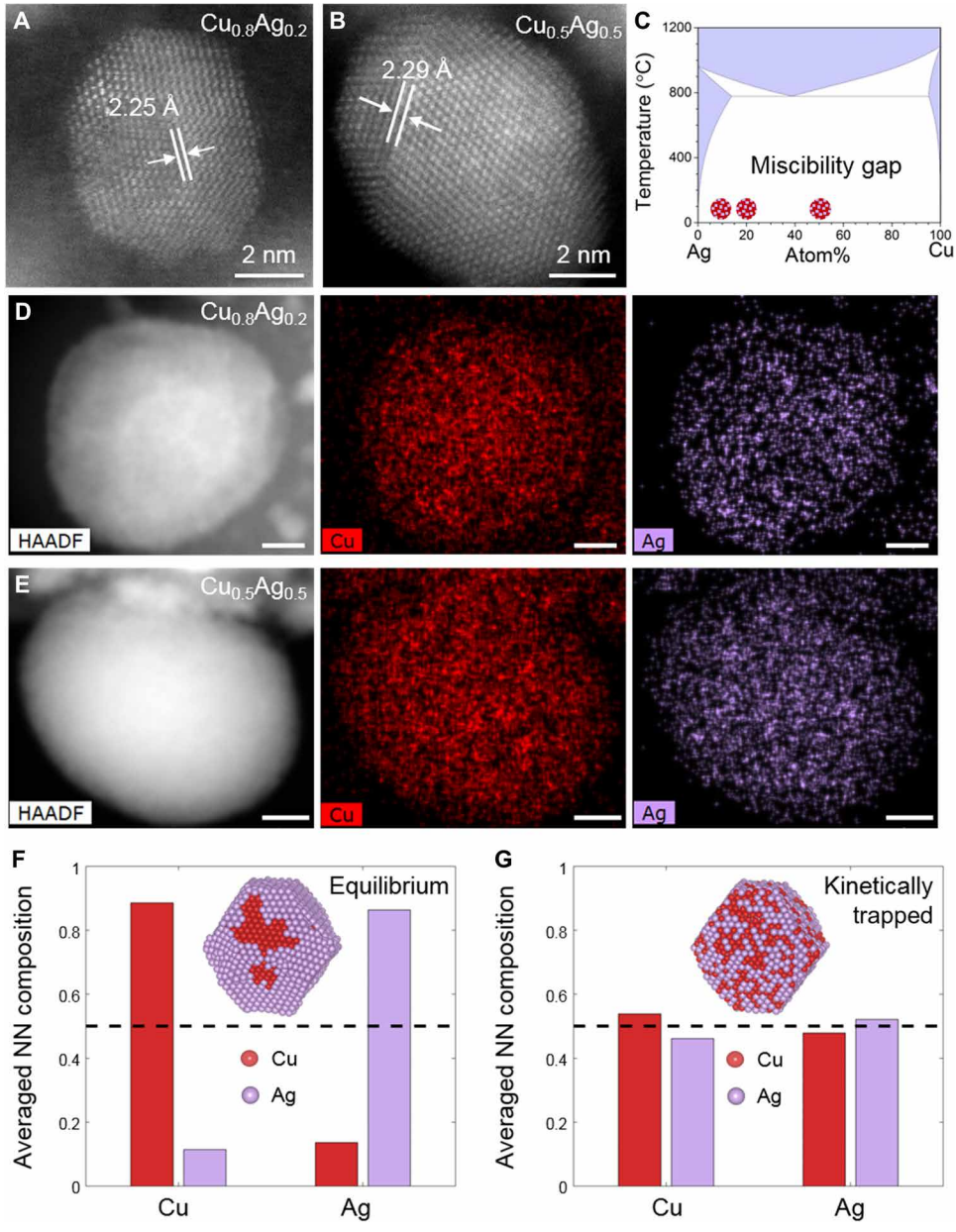

Fig. 3. Alloyed Cu-Ag bimetallics with different compositions. High-resolution STEM image of typical (**A**) $Cu_{0.8}Ag_{0.2}$ and (**B**) $Cu_{0.5}Ag_{0.5}$ nanoparticles. (**C**) Bulk phase diagram of Cu-Ag, in which the $Cu_{1-x}Ag_x$ bimetallics in this work fall in the miscibility gap. Phase diagram of Cu-Ag reproduced from (*15*). Copyright 2010, ASM International. HAADF-STEM images and EDS elemental mapping of (**D**) $Cu_{0.8}Ag_{0.2}$ and (**E**) $Cu_{0.5}Ag_{0.5}$ nanoparticles. Scale bars, 5 nm. Structure modeling of the $Cu_{0.5}Ag_{0.5}$ nanoparticle and the statistical analysis of the averaged nearest-neighbor (NN) composition surrounding the Cu and Ag atoms after MD/MC simulation at 25°C, in which one MC trial step was attempted (**F**) every 1 fs to simulate sufficient diffusion for thermodynamic equilibrium and (**G**) every 10 ps to simulate limited diffusion and kinetic trapping.

coupled molecular dynamics (MD)/MC simulation at 25°C (see Materials and Methods for details). We investigated the structure of the modeled Cu-Ag nanoparticle under different diffusion conditions (by proposing one MC trial step every *n* MD time steps), calculating the averaged composition of the first-nearest-neighbor lattice sites around Cu and Ag (fig. S18). At the thermodynamic equilibrium state (simulated with $n = 1$ fs, sufficient diffusion), approximately 88% of the nearest-neighbor atoms around Cu are Cu atoms, and, similarly, Ag has higher affinity to Ag atoms (Fig. 3F), which indicates a phase segregation between Cu and Ag. The equilibrium structure of the Cu-Ag nanoparticle is phase segregated (Cu core and Ag shell structure as shown in Fig. 3F, inset), in good agreement with most reported Cu-Ag nanostructures synthesized by equilibrium methods (*19*, *20*). In contrast, using the nonequilibrium synthesis described in this work, the quenched Cu-Ag nanoparticle was kinetically trapped, allowing limited diffusion ($n = 10$ ps). As a result, the average probability of Cu-Cu, Ag-Ag, and Cu-Ag neighbor pairs is approximately equal to 0.5 (Fig. 3G), indicating homogeneous mixing of the Cu and Ag atoms in the $Cu_{0.5}Ag_{0.5}$ bimetallic nanoparticle. Therefore, our simulation results confirm that the nonequilibrium

synthesis can trap the bimetallic mixture in homogeneous nanoparticles (Fig. 3G, inset) that are stable at room temperature due to limited diffusion.

The as-synthesized nonequilibrium Cu-X bimetallic nanoparticles are further investigated as electrocatalysts for carbon monoxide reduction (COR). Electrochemical reduction of CO_2 (CO_2R) or CO_2-derived CO is particularly attractive for sustainable chemical productions because if powered by renewable electricity, then the whole process does not emit any greenhouse gas CO_2 (sometimes even with a negative CO_2 emission) (*22*–*25*). Although much effort has been devoted to developing Cu-X bimetallic catalysts toward C_{2+} products in CO_2R/COR, a comprehensive understanding of structure-property correlation is largely lacking because of the highly heterogeneous nature of Cu-X bimetallic nanomaterials (such as core-shell and phase segregation). Here, the newly synthesized homogeneously alloyed Cu-X samples enable us to screen a large set of bimetallics with different compositions but a nearly identical nanostructure.

The COR experiments were conducted in 1 M potassium hydroxide (KOH) using a three-compartment flow electrolyzer (fig. S19) (*25*). High current densities (>100 mA cm^{-2}) are achieved for all $Cu_{0.9}X_{0.1}$ bimetallics and pure Cu catalysts (fig. S20). As shown in Fig. 4A, the major COR products are acetate and ethylene, while the minor products are propanol, ethanol, and methane (see figs. S21 and S22 and tables S1 and S2 for detail). Compared with pure Cu, $Cu_{0.9}Ni_{0.1}$ and $Cu_{0.9}Ag_{0.1}$ exhibit notably enhanced C_{2+} products and suppressed H_2 FE, while $Cu_{0.9}Sn_{0.1}$ has negative effect and other metals have minimal effect. The trend is maintained over a broad range of applied potentials (figs. S23 and S24). In particular, $Cu_{0.9}Ni_{0.1}$ shows ~20% improvement in C_{2+} FE, showing the highest C_{2+} FE of ~76 and ~40% suppression in H_2 FE compared with that of Cu. Notably, $Cu_{0.9}Ni_{0.1}$ exhibits an exceptionally high maximum acetate FE of ~47% with a specific current density of ~93 mA cm^{-2}, which is among the highest values reported to date for acetate formation in COR in the literature (Fig. 4B and table S3) (*25*–*29*).

To compare the intrinsic reaction rates of different bimetallics to pure Cu, the current densities were normalized to the electrochemically active surface area (ECSA) (figs. S25 and S26). We note that the ECSA-normalized activity for bimetallics in COR is a conservative estimate as not all the metal sites are expected to be active. Nonetheless, the intrinsic reaction rates of bimetallic catalysts were either comparable or slightly enhanced, indicating the promotional role of secondary metals on Cu. In addition, phase-segregated $Cu_{0.9}Ni_{0.1}$ and $Cu_{0.9}Ag_{0.1}$ prepared via conventional thermal annealing have been evaluated in COR to illustrate the effect of mixing patterns (fig. S27 and table S4). Compared with homogeneously mixed alloys, phase-segregated alloys exhibit higher H_2 and lower C_{2+} FE (figs. S28 and S29). Metals such as Ni and Ag as single metals are poor catalysts in COR (*30*), and synergistic effect on bimetallics is realized when the interaction between Cu and secondary metal is maximized via homogenous mixing.

To investigate the origin of the enhanced performance on homogeneous $Cu_{0.9}Ni_{0.1}$ and $Cu_{0.9}Ag_{0.1}$, we used in situ attenuated total reflection surface enhanced infrared absorption spectroscopy (ATR-SEIRAS). The strength of the CO adsorption is reflected on the position of the CO adsorption peak (*31*), and the in situ ATR-SEIRAS study at −0.4 V versus reversible hydrogen electrode (RHE) reveals the CO adsorption strength of various catalysts under COR operating condition (fig. S30). The spectra show a shift in the adsorbed CO band center from 2053 cm^{-1} on Cu to much lower 2040 cm^{-1}

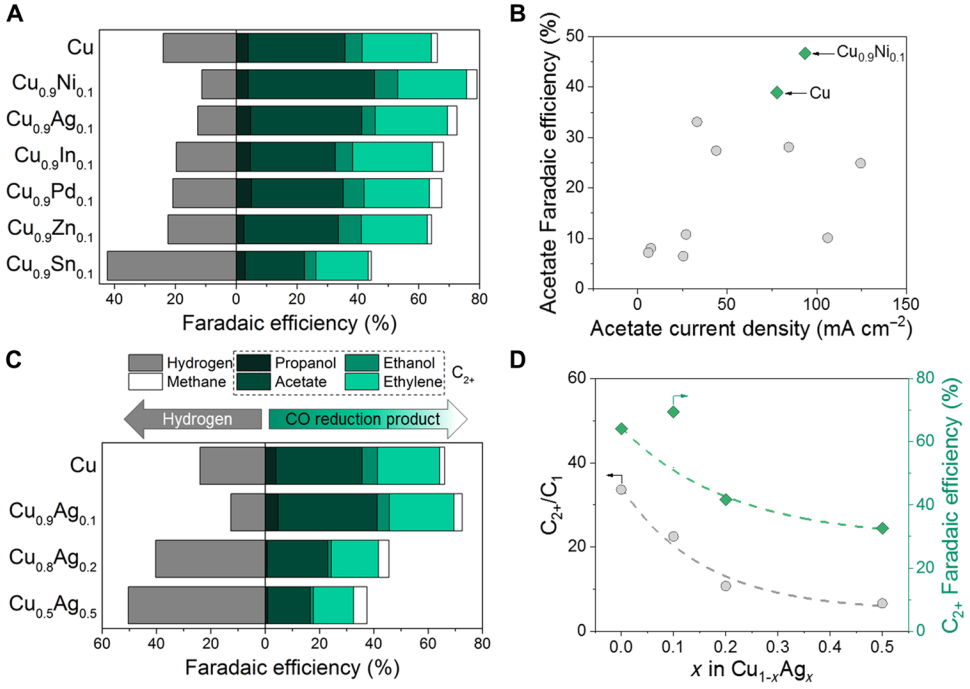

Fig. 4. Bimetallic catalyst screening for the COR. (**A**) FE of pure Cu and different $Cu_{0.9}X_{0.1}$ bimetallic catalysts at −0.70 ± 0.01 V versus RHE. (**B**) The acetate FE and current densities of the Cu-X bimetallic and Cu catalysts in this work compared with state-of-the-art catalysts in COR in 1 M KOH/NaOH (*25*–*29*). (**C**) FE of $Cu_{1-x}Ag_x$ bimetallics with different atom ratios and pure Cu at −0.70 ± 0.01 V versus RHE. (**D**) The C_{2+}/C_1 FE ratio and C_{2+} FE of $Cu_{1-x}Ag_x$ bimetallics with different atom ratios and pure Cu at −0.70 ± 0.01 V versus RHE.

on $Cu_{0.9}Ni_{0.1}$. A peak shift to a lower wave number indicates an enhanced CO adsorption on $Cu_{0.9}Ni_{0.1}$. Because Ni has stronger CO binding energy than Cu and the modification in the electronic structure of bimetallic catalysts generally trends with the property of the secondary metal (*32*), the incorporation of Ni likely strengthens the interaction between the adsorbate and the catalyst surface. In contrast, $Cu_{0.9}Ag_{0.1}$ exhibits a similar band center to that of Cu at 2052 cm^{-1} despite the similarly enhanced performance. Although stronger CO binding energy may be responsible for the enhanced performance on $Cu_{0.9}Ni_{0.1}$, further investigation is needed to determine the origin of performance enhancement of $Cu_{0.9}Ag_{0.1}$ in COR.

The nonequilibrium synthesis that enables free mixing of immiscible elements at any composition allows us to investigate the composition effect of immiscible bimetallics on catalysis, which cannot be achieved via conventional methods. For instance, Kenis and co-workers (*5*) and Bell and co-workers (*17*) reported enhanced selectivity toward C_{2+} products in CO_2R using Cu-Ag alloys synthesized via arc meting and galvanic replacement and electrodeposition, respectively. However, because of the limitation of these synthesis methods, those catalysts were either phase segregated or partially alloyed, leaving the understanding of the composition-property relationship incomplete. Thus, we investigated the effect of the Cu-Ag bimetallic composition on COR to fill this knowledge gap (see figs. S31 and S32 and tables S1 and S5 for more detail). As shown in Fig. 4C, COR products and H_2 FEs vary notably with different concentrations of Ag. The total COR FE increases with decreasing concentration of Ag from $Cu_{0.5}Ag_{0.5}$ to Cu except for $Cu_{0.9}Ag_{0.1}$, which exhibits the highest C_{2+} FE, while the opposite trend is observed for H_2 FE. The trend is maintained over a wide range of applied potentials (figs. S33 and S34). We also report the ECSA-normalized current densities (figs. S35 and S36), and the intrinsic reaction rates are slightly improved for Cu-Ag bimetallics.

While the ratio of C_{2+} to C_1 product decreases with increasing concentration of Ag, the highest C_{2+} FE was achieved on $Cu_{0.9}Ag_{0.1}$ (Fig. 4D). As evidenced by the increasing trend of CH_4 FE with increasing concentration of Ag (fig. S37), the presence of Ag atoms interferes with the capability of Cu to dimerize CO intermediates and promotes CH_4 formation. This is in agreement with a previous study suggesting that C-C coupling is favored on neighboring Cu sites (*33*). In contrast, the interaction between Cu and Ag is expected to increase with increasing concentration of Ag, yielding greater modification on the property of Cu. Collectively, these results suggest that geometric and electronic effects compete with each other in the Cu-Ag bimetallic catalysts, and the best performance is realized with $Cu_{0.9}Ag_{0.1}$ when there is an optimal balance. We propose that to design efficient catalysts toward C_{2+} products, it is vital to incorporate an optimal amount of secondary metal while maintaining neighboring Cu sites. The elucidation of the structure-property relationship of Cu-Ag bimetallics in COR, which has been lacking due to the miscibility gap in Cu-Ag bimetallics, is made possible by this unique nonequilibrium synthesis method.

To evaluate the stability of nonequilibrium bimetallic catalysts, we conducted a constant current COR experiment at 100 mA cm^{-2} for 3 hours using $Cu_{0.9}Ag_{0.1}$ and $Cu_{0.9}Ni_{0.1}$ as catalysts (fig. S38). FE and applied potentials were stable for both catalysts over the span of 3 hours. The structural stability was also examined via HAADF-STEM images and corresponding EDS elemental mapping of the catalysts after the stability test. A small portion of the $Cu_{0.9}Ag_{0.1}$ nanoparticles become phase segregated with Ag on the surface (due to the lower surface energy of Ag), whereas the majority remains homogeneously mixed (fig. S39). For $Cu_{0.9}Ni_{0.1}$, there was no sign of phase segregation after COR (fig. S40). Although we observe a slight indication of phase segregation on $Cu_{0.9}Ag_{0.1}$, these results suggest that the majority of the $Cu_{0.9}Ag_{0.1}$ and $Cu_{0.9}Ni_{0.9}$ catalysts remain homogenous under reaction conditions.

CONCLUSION

We demonstrate the ability of the nonequilibrium synthetic strategy to overcome the immiscibility of Cu-based bimetallics. As a proof of concept, we successfully prepared a collection of homogeneous Cu-X alloys, including "immiscible" combinations, such as Cu-Ag, to create a library of bimetallic materials that enable the systematic study of the role of secondary metals and screening of various Cu-X bimetallics in COR at commercially relevant current densities. Among various Cu-X alloys, $Cu_{0.9}Ni_{0.1}$ and $Cu_{0.9}Ag_{0.1}$ exhibited enhanced FE toward C_{2+} products. In particular, $Cu_{0.9}Ni_{0.1}$ showed the highest C_{2+} product FE of ~76%, which is ~20% higher compared with that of Cu. The $Cu_{0.9}Ni_{0.1}$ also demonstrated an exceptionally high maximum acetate FE of ~47% with specific current densities of ~93 mA cm^{-2}, among the highest values reported to date. Moreover, we elucidated the structure-property relationship of Cu-Ag bimetallics and find that incorporating an optimal amount of secondary metal while maintaining neighboring Cu sites is essential for effective catalyst design for COR. The nonequilibrium synthetic strategy should not be limited to Cu-based bimetallics and can be extended to other bimetallic or metal oxide systems. Together with artificial intelligence–based machine learning, the new synthetic method will make rapid catalyst screening and rational design possible.

MATERIALS AND METHODS

Synthesis

The process for the nonequilibrium synthesis was realized using a high-temperature shock method on CNF substrates, as first demonstrated by Chen *et al.* in 2016 (*34*). The CNFs were prepared by electrospinning polyacrylonitrile. The polyacrylonitrile solution in dimethylformamide (10 wt %) was electrospun from a syringe at a rate of 1 ml $hour^{-1}$ controlled by a peristaltic pump. The needle of the syringe was placed 15 cm from a rotating aluminum foil, between which a high voltage of 10 kV was applied. The as-spun polyacrylonitrile nanofiber mat was peeled off from the aluminum foil after electrospinning and calcined in air at 260°C for 5 hours, then carbonized in argon flow at 900°C for 2 hours, and lastly treated in CO_2 flow at 750°C for 2 hours to obtain the CNFs.

To prepare the Cu-X (X = Ag, Ni, Sn, etc.) bimetallic nanoparticles, the CNF mat was attached between two Cu electrodes using silver paste. The precursor solutions of Cu and X (0.05 M nitrate salt dissolved in ethanol) were mixed and dispersed in the CNF substrate. The material was then dried at 80°C and moved into an argon-filled glovebox. An external power source (Keithley 2425) connected to the Cu electrodes was used to create a rapid current pulse (0.2 s) through the CNF substrate. The Joule heating induced by the current pulse instantly elevated the temperature of the CNFs (accompanied with the emission of light) and then rapidly quenched after the current pulse ended. The metal nitrates decomposed during the high-temperature shock and were mixed and trapped in bimetallic nanoparticles after the rapid quench.

Characterization

The temperature evolution during the high-temperature shock synthesis was measured by recording the color ratio pyrometry using a Vision Research Phantom Miro M110 high-speed camera (2000 frames per s). For the temperature calculation, the gray-body model was applied, substituted into Planck's law, and integrated over the entire spectrum to which the camera was sensitive. MATLAB was used to extract raw pixel values and calculate the temperatures. Three color ratios (red, green, and blue) were simultaneously used to estimate the temperature by minimizing their summed error with a further thresholding used to eliminate summed errors.

The particle morphology of the Cu-X alloys was observed on a Hitachi SU-70 field emission SEM coupled with an EDS system for elemental analysis. TEM images of the Cu-X nanoparticles were measured with a JEOL 2100F TEM. STEM-EDS elemental maps of Cu-X alloys were acquired with a Thermo Fisher Scientific Talos F200X. High-resolution STEM images were acquired with a Hitachi HD2700C dedicated STEM with a probe corrector. In situ STEM and EDS line scan were performed at room temperature, 250°C, 500°C, and 1000°C with a Wildfire in situ heating system. The EDS was obtained at each temperature after stabilizing for 10 min. We note that the EDS for 1000°C was taken after holding at 1000°C for 10 min and cooling to room temperature because EDS could not be done at 1000°C. All TEM were operated at an accelerating voltage of 200 kV. Thermogravimetric analysis was performed on a Discovery SDT 650 thermal analyzer in air from room temperature to 800°C with a temperature ramp rate of 10°C/min. XRD of the bimetallic nanoparticles was conducted on a D8 Advance Diffractometer (Bruker) at 40 kV and 40 mA using a Cu Kα radiation source (λ = 1.54056 Å).

The ECSA was determined by measuring the double-layer capacitance (C_{DL}) of Cu-X alloys and Cu nanoparticles in Ar-purged 0.1 M $HClO_4$ in an H cell. All electrodes were electrochemically reduced at 5 mA cm^{-2} for 10 min before ECSA measurements. Cyclic voltammetry was performed in a non-Faradaic potential region at various scan rates from 5 to 50 mV s^{-1}, and the observed currents were plotted as a function of scan rate. C_{DL} was determined by obtaining the slope, and ECSA was calculated by normalizing to the C_{DL} of $Cu_{0.9}Ag_{0.1}$.

Electrode preparation

Cu-based bimetallics and Cu nanoparticles were ground into fine powders. The cathode catalyst inks were prepared by dissolving 3 mg of the catalyst in 3 μl of Nafion solution (5 wt % in 50/50 water and isopropanol) and 1.44 ml of isopropanol. IrO_2 powder (99.99%) was purchased from Alfa Aesar, and the anode catalyst ink was prepared by dissolving 25 mg of IrO_2 in 20 μl of Nafion solution and 3 ml of isopropanol. The catalyst inks were sonicated for at least 30 min before drop casting. Then, 0.17, 0.34, and 0.25 mg cm^{-2} of the catalysts prepared via thermal shock, catalysts prepared via conventional thermal annealing, and IrO_2 catalysts, respectively, were drop casted onto a Sigracet 29 BC gas diffusion layer (Fuel Cell Store). The loading of the catalysts prepared via conventional thermal annealing was double the loading of the catalysts prepared via thermal shock to access similar potential range in COR.

Electrocatalytic performance measurement

The CO electrolysis was performed in a three-channel flow cell configuration with channel dimensions of 2 cm by 0.5 cm by 0.15 cm. A FAA-3 hydroxide exchange membrane (Fumatech) was used to separate the cathode and anode chambers. CO gas was flowed at 15 standard cubic centimeters per minute via a mass flow controller (Brooks GF40). KOH (1 M; 99.99%; Sigma-Aldrich) was used as catholyte, while lower-purity 1 M KOH (85%; Sigma-Aldrich) was used as anolyte. Higher-purity KOH was used as the catholyte since metal impurities are known to severely affect the COR performance at the cathode. Both catholyte and anolyte were flowed at 0.9 ml min^{-1} via peristaltic pumps. The pressure of the gas in the gas chamber was controlled via a backpressure controller (Cole-Parmer).

Chronopotentiometry experiments were conducted via an AutoLab PG128N. The catalysts were reduced at 100 mA cm^{-2} for 20 min before measurements, and each current was applied for 20 min for product quantification. Every experiment was repeated three times. The half-cell potentials were measured at constant current densities after the cell had reached steady state using an external Ag/AgCl reference electrode (Pine Research). The resistance between the working and the reference electrode was measured with the current-interrupt technique, and the measured potential was corrected for the resistance. The cathode potentials were reported with respect to the IR-corrected RHE in which E (versus RHE) = E (versus Ag/AgCl) + 0.209 V + 0.0591 V/pH × pH − η_{IRdrop}.

The gas products were quantified using a Multiple Gas Analyzer #5 gas chromatography system (SRI Instruments) equipped with Molseive 5A and HayeSep D columns connected to a thermal conductivity detector and a flame ionization detector. The liquid products were quantified via ^1H nuclear magnetic resonance (NMR) with water suppression using a presaturation method (Bruker AVIII 600 MHz NMR spectrometer). Typically, collected liquid products were diluted, and 500 μl of diluted sample was mixed with 100 μl of D_2O containing 25 ppm (v/v) dimethyl sulphoxide (99.9%; Alfa Aesar) as the internal standard.

In situ ATR-SEIRAS

A two compartment polytetrafluoroethylene cell with three electrodes was used for ATR-SEIRAS measurements. The schematic of the cell and steps to prepare chemically deposited gold film on the silicon ATR crystals can be found in our previous study (*35*). The working electrode was the bimetallic catalyst drop casted on the gold film on the silicon ATR crystals with catalyst loading of 0.4 to 0.5 mg cm^{-2}. The catalyst inks were prepared by dissolving 5 mg of catalyst in 1 μl of Nafion solution (5 wt % in 50/50 water and isopropanol) and 250 μl of isopropanol. A graphite counter electrode was placed in one compartment, and a working electrode and Ag/AgCl reference electrode (3.0 M NaCl, BASi) were placed in the other compartment with gas inlet and purge lines. Two compartments were separated by a Nafion ion exchange membrane (Nafion 211, Fuel Cell Store). Potassium hydroxide solution (0.1 M; Sigma-Aldrich; 99.99%) was used as the electrolyte. The electrodes were connected to a potentiostat (Solartron 1260/1287) to apply potentials during measurements. The cell is integrated into the Agilent Technologies Cary 660 FTIR spectrometer equipped with a liquid nitrogen–cooled mercury-cadmium-telluride detector. All spectra were collected with 64 coadded scans and 4 cm^{-1} resolutions.

Simulation

To simulate the thermal shock synthesis of the Cu-Ag nanoparticles at high temperature, a Metropolis algorithm–based MC simulation method was used to sample the atomic configurations of the Cu-Ag alloy nanoparticle in canonical ensemble (*36*, *37*). Starting from a

random atomic configuration, 5 million MC trial steps that swap the position of Cu and Ag atoms were attempted to simulate the long-range diffusion process in the modeled system. At given temperature T, the transition probability p from the old configuration to the new configuration was calculated according to the Boltzmann distribution

$$p = \min\left[1, \exp\left(-\frac{\Delta E}{k_B T}\right)\right]$$

in which ΔE is the total energy change for the configuration transition of the alloy system and k_B is the Boltzmann constant.

The structures of the Cu-Ag alloy nanoparticles at room temperature were investigated by a coupled MD/MC simulation scheme. The samples were held for 10 ns in the MD simulation, during which one MC trial step was inserted every n time steps, with n ranging from 1 fs to 10 ps. Smaller n represents that the diffusion between the Cu and Ag occurs more frequently within the MD simulation time scale. The MD/MC simulations were executed in nvt ensemble with a Nosé-Hoover thermostat (*38*). The velocity Verlet algorithm was used to integrate the equation of motion with a time step of 1 fs. All the simulations were run in the Large-scale Atomic/Molecular Massively Parallel Simulator package (*39*).

The interatomic potential of the Cu-Ag alloy system was described within the framework of the second-nearest-neighbor modified embedded atom method (MEAM) (*40*, *41*). The parameters of the MEAM potentials for pure elements Cu, Ag, and Cu-Ag binary alloys were taken from reference (*42*, *43*).

SUPPLEMENTARY MATERIALS

Supplementary material for this article is available at http://advances.sciencemag.org/cgi/content/full/6/17/eaaz6844/DC1

REFERENCES AND NOTES

1. K. D. Gilroy, A. Ruditskiy, H.-C. Peng, D. Qin, Y. Xia, Bimetallic nanocrystals: Syntheses, properties, and applications. *Chem. Rev.* **116**, 10414–10472 (2016).
2. D. Wang, Y. Li, Bimetallic nanocrystals: Liquid-phase synthesis and catalytic applications. *Adv. Mater.* **23**, 1044–1060 (2011).
3. J. Xu, T. White, P. Li, C. He, J. Yu, W. Yuan, Y.-F. Han, Biphasic Pd–Au alloy catalyst for low-temperature CO oxidation. *J. Am. Chem. Soc.* **132**, 10398–10406 (2010).
4. F. Besenbacher, I. Chorkendorff, B. S. Clausen, B. Hammer, A. M. Molenbroek, J. K. Nørskov, I. Stensgaard, Design of a surface alloy catalyst for steam reforming. *Science* **279**, 1913–1915 (1998).
5. T. T. H. Hoang, S. Verma, S. Ma, T. T. Fister, J. Timoshenko, A. I. Frenkel, P. J. A. Kenis, A. A. Gewirth, Nanoporous copper–silver alloys by additive-controlled electrodeposition for the selective electroreduction of CO_2 to Ethylene and Ethanol. *J. Am. Chem. Soc.* **140**, 5791–5797 (2018).
6. G. Chen, N. Zou, B. Chen, J. B. Sambur, E. Choudhary, P. Chen, Bimetallic effect of single nanocatalysts visualized by super-resolution catalysis imaging. *ACS Cent. Sci.* **3**, 1189–1197 (2017).
7. L. Li, L. Zhou, S. Ould-Chikh, D. H. Anjum, M. B. Kanoun, J. Scaranto, M. N. Hedhili, S. Khalid, P. V. Laveille, L. D'Souza, A. Clo, J.-M. Basset, Controlled surface segregation leads to efficient coke-resistant nickel/platinum bimetallic catalysts for the dry reforming of methane. *ChemCatChem* **7**, 819–829 (2015).
8. A. Wong, Q. Liu, S. Griffin, A. Nicholls, J. R. Regalbuto, Synthesis of ultrasmall, homogeneously alloyed, bimetallic nanoparticles on silica supports. *Science* **358**, 1427–1430 (2017).
9. N. P. Mankad, Selectivity effects in bimetallic catalysis. *Chem. A Eur. J.* **22**, 5822–5829 (2016).
10. M. Sankar, N. Dimitratos, P. J. Miedziak, P. P. Wells, C. J. Kiely, G. J. Hutchings, Designing bimetallic catalysts for a green and sustainable future. *Chem. Soc. Rev.* **41**, 8099–8139 (2012).
11. Z. Zhang, T. M. Nenoff, J. Y. Huang, D. T. Berry, P. P. Provencio, Room temperature synthesis of thermally immiscible Ag–Ni nanoalloys. *J. Phys. Chem. C* **113**, 1155–1159 (2009).
12. N. S. Tabrizi, Q. Xu, N. M. van der Pers, A. Schmidt-Ott, Generation of mixed metallic nanoparticles from immiscible metals by spark discharge. *J. Nanopart. Res.* **12**, 247–259 (2010).
13. K. A. Kane, A. C. Reber, S. N. Khanna, M. F. Bertino, Laser synthesized nanoparticle alloys of metals with bulk miscibility gaps. *Prog. Nat. Sci: Mater. Int.* **28**, 456–463 (2018).
14. U. Aslam, S. Linic, Kinetic trapping of immiscible metal atoms into bimetallic nanoparticles through plasmonic visible light-mediated reduction of a bimetallic oxide precursor: Case study of Ag–Pt nanoparticle synthesis. *Chem. Mater.* **28**, 8289–8295 (2016).
15. H. Okamoto, *Phase Diagrams for Binary Alloys* (ASM International, ed. 2, 2010).
16. R. Ferrando, J. Jellinek, R. L. Johnston, Nanoalloys: From theory to applications of alloy clusters and nanoparticles. *Chem. Rev.* **108**, 845–910 (2008).
17. E. L. Clark, C. Hahn, T. F. Jaramillo, A. T. Bell, Electrochemical CO_2 reduction over compressively strained CuAg surface alloys with enhanced multi-carbon oxygenate selectivity. *J. Am. Chem. Soc.* **139**, 15848–15857 (2017).
18. K. E. Dettelbach, J. He, N. J. J. Johnson, A. Huang, A. Bottomley, B. Lam, D. A. Salvatore, C. P. Berlinguette, Kinetic phases of Ag–Cu alloy films are accessible through photodeposition. *J. Mater. Chem. A* **7**, 711–715 (2019).
19. W. T. Osowiecki, X. Ye, P. Satish, K. C. Bustillo, E. L. Clark, A. P. Alivisatos, Tailoring morphology of Cu–Ag nanocrescents and core–shell nanocrystals guided by a thermodynamic model. *J. Am. Chem. Soc.* **140**, 8569–8577 (2018).
20. A. Rapallo, G. Rossi, R. Ferrando, A. Fortunelli, B. C. Curley, L. D. Lloyd, G. M. Tarbuck, R. L. Johnston, Global optimization of bimetallic cluster structures. I. Size-mismatched Ag–Cu, Ag–Ni, and Au–Cu Systems. *J. Chem. Phys.* **122**, 194308 (2005).
21. W. Wu, M. Lei, S. Yang, L. Zhou, L. Liu, X. Xiao, C. Jiang, V. A. L. Roy, A one-pot route to the synthesis of alloyed Cu/Ag bimetallic nanoparticles with different mass ratios for catalytic reduction of 4-nitrophenol. *J. Mater. Chem. A* **3**, 3450–3455 (2015).
22. Q. Lu, F. Jiao, Electrochemical CO_2 reduction: Electrocatalyst, reaction mechanism, and process engineering. *Nano Energy* **29**, 439–456 (2016).
23. W. Zhu, R. Michalsky, Ö. Metin, H. Lv, S. Guo, C. J. Wright, X. Sun, A. A. Peterson, S. Sun, Monodisperse Au Nanoparticles for Selective Electrocatalytic Reduction of CO_2 to CO. *J. Am. Chem. Soc.* **135**, 16833–16836 (2013).
24. Q. Lu, J. Rosen, Y. Zhou, G. S. Hutchings, Y. C. Kimmel, J. G. Chen, F. Jiao, A selective and efficient electrocatalyst for carbon dioxide reduction. *Nat. Commun.* **5**, 3242 (2014).
25. M. Jouny, W. Luc, F. Jiao, High-rate electroreduction of carbon monoxide to multi-carbon products. *Nat. Catal.* **1**, 748–755 (2018).
26. W. Luc, X. Fu, J. Shi, J.-J. Lv, M. Jouny, B. H. Ko, Y. Xu, Q. Tu, X. Hu, J. Wu, Q. Yue, Y. Liu, F. Jiao, Y. Kang, Two-dimensional copper nanosheets for electrochemical reduction of carbon monoxide to acetate. *Nat. Catal.* **2**, 423–430 (2019).
27. D. S. Ripatti, T. R. Veltman, M. W. Kanan, Carbon monoxide gas diffusion electrolysis that produces concentrated C_2 products with high single-pass conversion. *Joule* **3**, 240–256 (2019).
28. T.-T. Zhuang, Y. Pang, Z.-Q. Liang, Z. Wang, Y. Li, C.-S. Tan, J. Li, C. T. Dinh, P. De Luna, P.-L. Hsieh, T. Burdyny, H.-H. Li, M. Liu, Y. Wang, F. Li, A. Proppe, A. Johnston, D.-H. Nam, Z.-Y. Wu, Y.-R. Zheng, A. H. Ip, H. Tan, L.-J. Chen, S.-H. Yu, S. O. Kelley, D. Sinton, E. H. Sargent, Copper nanocavities confine intermediates for efficient electrosynthesis of C3 alcohol fuels from carbon monoxide. *Nat. Catal.* **1**, 946–951 (2018).
29. J. Li, F. Che, Y. Pang, C. Zou, J. Y. Howe, T. Burdyny, J. P. Edwards, Y. Wang, F. Li, Z. Wang, P. De Luna, C.-T. Dinh, T.-T. Zhuang, M. I. Saidaminov, S. Cheng, T. Wu, Y. Z. Finfrock, L. Ma, S.-H. Hsieh, Y.-S. Liu, G. A. Botton, W.-F. Pong, X. Du, J. Guo, T.-K. Sham, E. H. Sargent, D. Sinton, Copper adparticle enabled selective electrosynthesis of n-propanol. *Nat. Commun.* **9**, 4614 (2018).
30. H. Yoshio, M. Akira, T. Ryutaro, S. Shin, Electrochemical reduction of carbon monoxide to hydrocarbons at various metal electrodes in aqueous solution. *Chem. Lett.* **16**, 1665–1668 (1987).
31. G. Bistoni, S. Rampino, N. Scafuri, G. Ciancaleoni, D. Zuccaccia, L. Belpassi, F. Tarantelli, How π back-donation quantitatively controls the CO stretching response in classical and non-classical metal carbonyl complexes. *Chem. Sci.* **7**, 1174–1184 (2016).
32. T. Bligaard, J. K. Nørskov, Ligand effects in heterogeneous catalysis and electrochemistry. *Electrochim. Acta* **52**, 5512–5516 (2007).
33. S. Ma, M. Sadakiyo, M. Heima, R. Luo, R. T. Haasch, J. I. Gold, M. Yamauchi, P. J. A. Kenis, Electroreduction of carbon dioxide to hydrocarbons using bimetallic Cu–Pd catalysts with different mixing patterns. *J. Am. Chem. Soc.* **139**, 47–50 (2017).
34. Y. Chen, G. C. Egan, J. Wan, S. Zhu, R. J. Jacob, W. Zhou, J. Dai, Y. Wang, V. A. Danner, Y. Yao, K. Fu, Y. Wang, W. Bao, T. Li, M. R. Zachariah, L. Hu, Ultra-fast self-assembly and stabilization of reactive nanoparticles in reduced graphene oxide films. *Nat. Commun.* **7**, 12332 (2016).
35. M. Dunwell, Q. Lu, J. M. Heyes, J. Rosen, J. G. Chen, Y. Yan, F. Jiao, B. Xu, The central role of bicarbonate in the electrochemical reduction of carbon dioxide on gold. *J. Am. Chem. Soc.* **139**, 3774–3783 (2017).
36. Z. Y. Liu, Y. K. Lei, C. Gray, G. F. Wang, Examination of solid-solution phase formation rules for high entropy alloys from atomistic Monte Carlo simulations. *JOM* **67**, 2364–2374 (2015).

37. G. F. Wang, M. A. Van Hove, P. N. Ross, M. I. Baskes, Monte Carlo simulations of segregation in Pt-Ni catalyst nanoparticles. *J. Chem. Phys.* **122**, 024706 (2005).
38. W. G. Hoover, Canonical dynamics: Equilibrium phase-space distributions. *Phys. Rev. A* **31**, 1695–1697 (1985).
39. S. Plimpton, Fast parallel algorithms for short-range molecular dynamics. *J. Comput. Phys.* **117**, 1–19 (1995).
40. M. I. Baskes, Modified embedded-atom potentials for cubic materials and impurities. *Phys. Rev. B* **46**, 2727–2742 (1992).
41. B.-J. Lee, M. I. Baskes, Second nearest-neighbor modified embedded-atom-method potential. *Phys. Rev. B* **62**, 8564–8567 (2000).
42. B.-J. Lee, J.-H. Shim, M. I. Baskes, Semiempirical atomic potentials for the fcc metals Cu, Ag, Au, Ni, Pd, Pt, Al, and Pb based on first and second nearest-neighbor modified embedded atom method. *Phys. Rev. B* **68**, 144112 (2003).
43. K.-H. Kang, I. Sa, J. C. Lee, E. Fleury, B. J. Lee, Atomistic modeling of the Cu-Zr-Ag bulk metallic glass system. *Scripta Mater.* **61**, 801–804 (2009).

Acknowledgments: We would like to thank D. Kline at the University of Maryland, College Park, for assistance in MATLAB coding for the high-temperature pulse measurement. **Funding:** This project is not directly funded. The authors at the University of Delaware thank the National Science Foundation for financial support (award no. CBET-1803200). This research used resources of the Center for Functional Nanomaterials, which is a U.S. DOE Office of Science Facility, at Brookhaven National Laboratory under contract no. DE-SC0012704. G.W. and Z.L. gratefully acknowledge the computational resources provided by the University of Pittsburgh Center for Research Computing as well as the Extreme Science and Engineering Discovery Environment (XSEDE), which is supported by National Science Foundation grant number ACI-1053575. **Author contributions:** C.Y., L.H., B.H.K., and F.J. designed the experiments. C.Y., M.C., Y.Y., and T.L. conducted the material synthesis and characterizations. B.H.K. and W.L. conducted the electrocatalytic performance measurement. S.H. and D.S. conducted the TEM and EDS characterization. Z.L. and G.W. conducted the atomistic simulation. A.S.M. and B.X. conducted the in situ ATR-SEIRAS experiment. X.W. contributed to the temperature measurement for the high-temperature shock synthesis. J.D. assisted in drawing schematics. C.Y., B.H.K., F.J., and L.H. collectively wrote the paper. All authors commented on the final manuscript. **Competing interests:** The authors declare that they have no competing interests. **Data and materials availability:** All data needed to evaluate the conclusions in the paper are present in the paper and/or the Supplementary Materials. Additional data related to this paper may be requested from the authors.

Submitted 1 October 2019
Accepted 28 January 2020
Published 24 April 2020
10.1126/sciadv.aaz6844

Citation: C. Yang, B. H. Ko, S. Hwang, Z. Liu, Y. Yao, W. Luc, M. Cui, A. S. Malkani, T. Li, X. Wang, J. Dai, B. Xu, G. Wang, D. Su, F. Jiao, L. Hu, Overcoming immiscibility toward bimetallic catalyst library. *Sci. Adv.* **6**, eaaz6844 (2020).

Science Advances

Overcoming immiscibility toward bimetallic catalyst library

Chunpeng Yang, Byung Hee Ko, Sooyeon Hwang, Zhenyu Liu, Yonggang Yao, Wesley Luc, Mingjin Cui, Arnav S. Malkani, Tangyuan Li, Xizheng Wang, Jiaqi Dai, Bingjun Xu, Guofeng Wang, Dong Su, Feng Jiao and Liangbing Hu

Sci Adv **6** (17), eaaz6844.
DOI: 10.1126/sciadv.aaz6844